

Reversible Thermosaliency of 4-Aminobenzonitrile

Lukman O. Alimi, Dewald P. van Heerden, Prem Lama, Vincent J. Smith and Leonard J. Barbour*

Department of Chemistry and Polymer Science University of Stellenbosch, Matieland, 7602, South Africa.

E-mail: ljb@sun.ac.za

Supplementary Information

Experimental Information

Materials

4-aminobenzonitrile was purchased from Sigma-Aldrich and used as received without further purification.

Crystallisation of 4-aminobenzonitrile (ABN)

Crystals of 4-aminobenzonitrile were obtained over several days by sublimation in a glass oven at 60 °C under dynamic vacuum (0.02 mbar). A small colourless crystal was selected for the variable-temperature single-crystal X-ray diffraction study of 4-aminobenzonitrile.

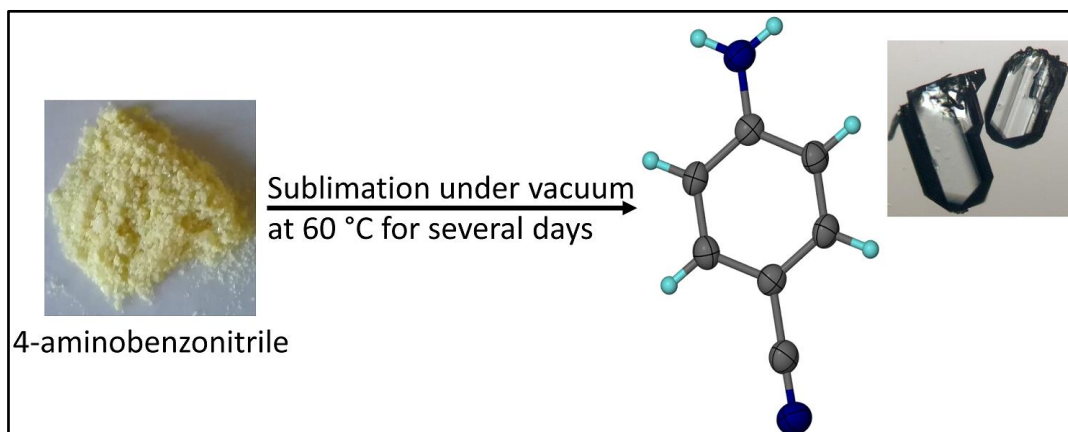


Fig. S1 Crystallisation of 4-aminobenzonitrile (ABN).

Differential Scanning Calorimetry (DSC)

DSC experiments were carried out using a TA Instruments DSC-Q100 equipped with a Liquid Nitrogen Cooling System (LNCS). Two different samples of ABN were used for the experiments: (i) a single crystal of 1.0 mg and (ii) 5.5 mg bulk crystals. In each case the sample was cooled in a standard hermetically sealed aluminium pan from 300 to 100 K and heated back to 300 K at the ramp rate of 5 K min⁻¹. Experiments were carried out under a constant flow of dry nitrogen gas at 50 ml min⁻¹. The enthalpies associated with the peaks were determined by integrating the baseline before and after the transition using the “integrate peak horizontal” command of the TA instruments Universal Analysis 2000 software.

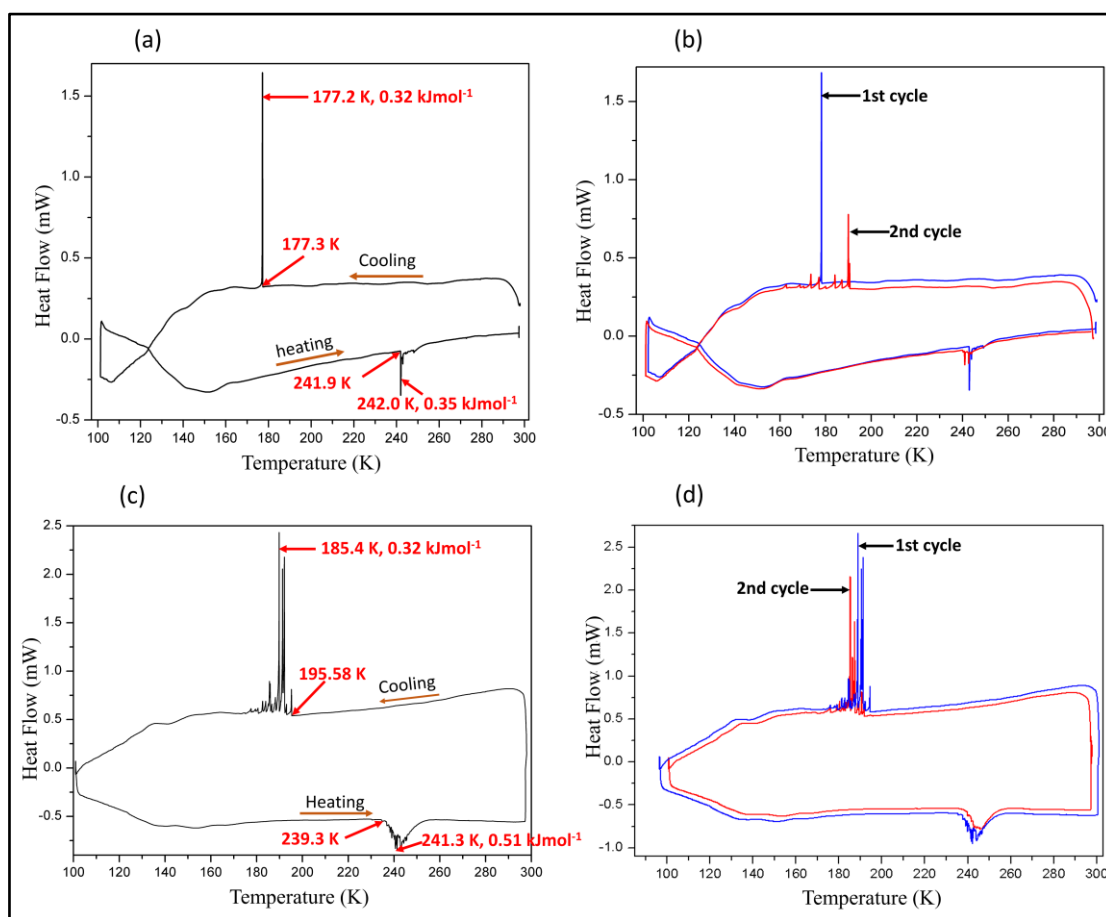


Fig. S2 DSC thermograms for ABN in the range 300 to 100 K. (a) A solitary exothermic peak is observed for a single crystal upon cooling, followed by a sawtooth-shaped endotherm upon heating. (b) Two cycles for the single crystal. (c) Sawtooth peaks during both cooling and heating for bulk crystals. (d) Two cycles for the bulk crystals.

Hot stage microscopy

The thermal behaviour of ABN was observed using a Linkam DSC-600 equipped with a Meiji MS-45D Unicam zoom macroscope and a PixelLink digital camera. A single crystal of ABN was cooled from 300 to 100 K and then heated back to 300 K at a constant rate of 5 K min⁻¹.

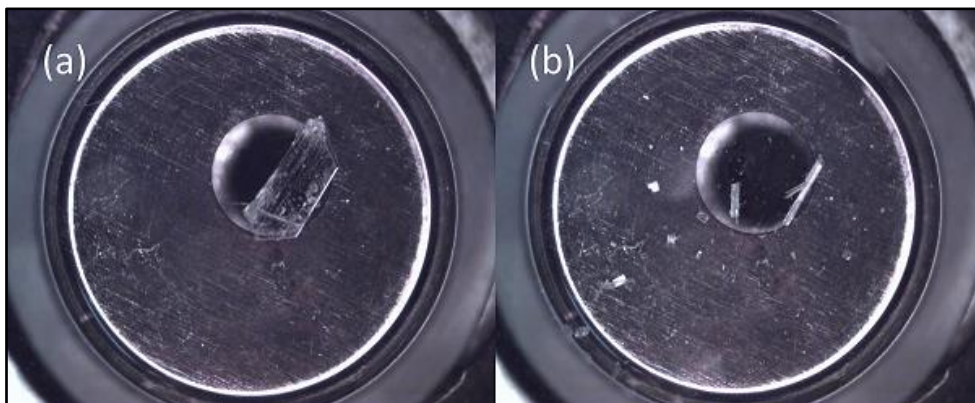


Fig. S3 Micrographs showing (a) a crystal of ABN before exploding and (b) the debris of the crystal after exploding during cooling from 300 to 100 K.

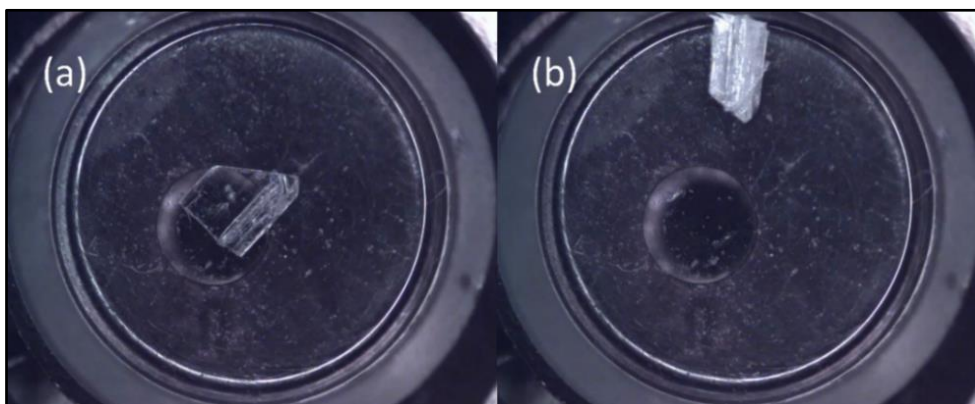


Fig. S4 Micrographs showing a crystal of coated in oil (a) before and (b) after the thermosalient event during cooling from 300 to 100 K.

Powder X-ray diffraction

Variable temperature powder X-ray diffraction data were recorded using Cu K α radiation ($\lambda = 1.5418 \text{ \AA}$, 40 kV and 30 mA) on a PANalytical X'pert PRO instrument operating in Bragg-Brentano geometry. The temperature was controlled by means of a short-nozzle Oxford Cryosystems Cryostream 700Plus cryostat. Samples were placed in sealed glass capillaries

(0.5mm) and data were recorded from 300 to 100 K at 20 K intervals. Pawley refinement was carried out using TOPAS¹ version 4.2.

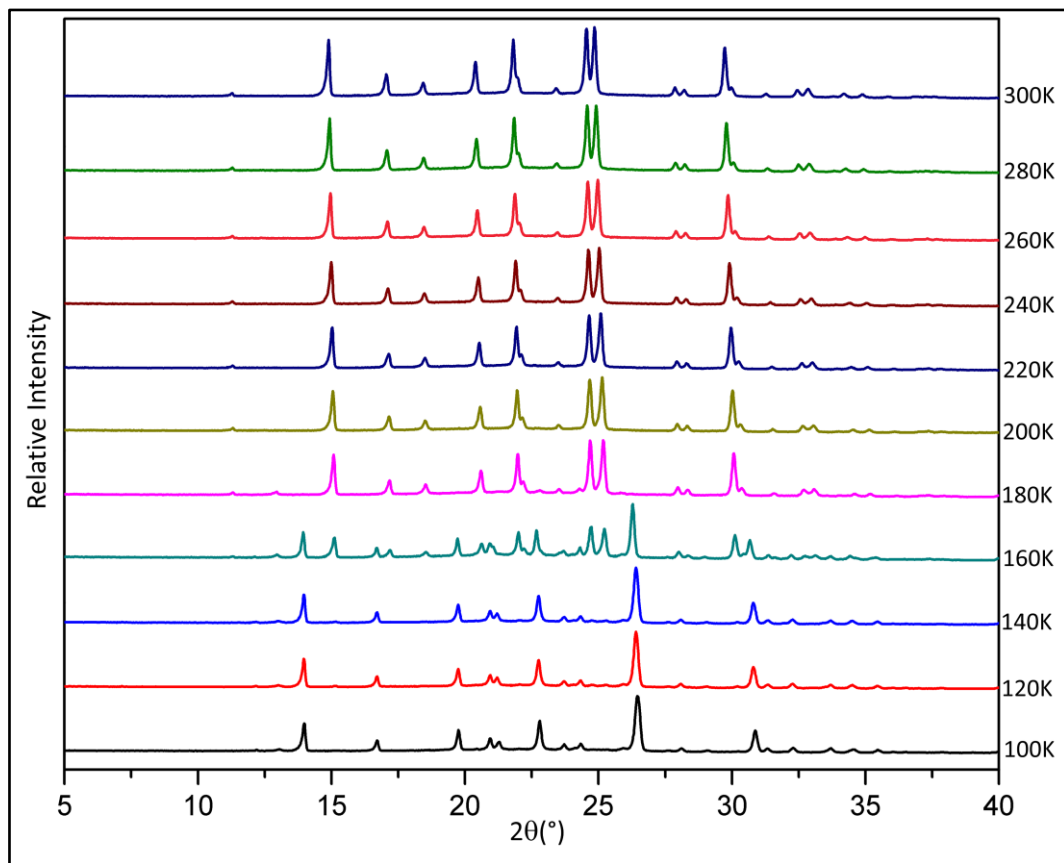
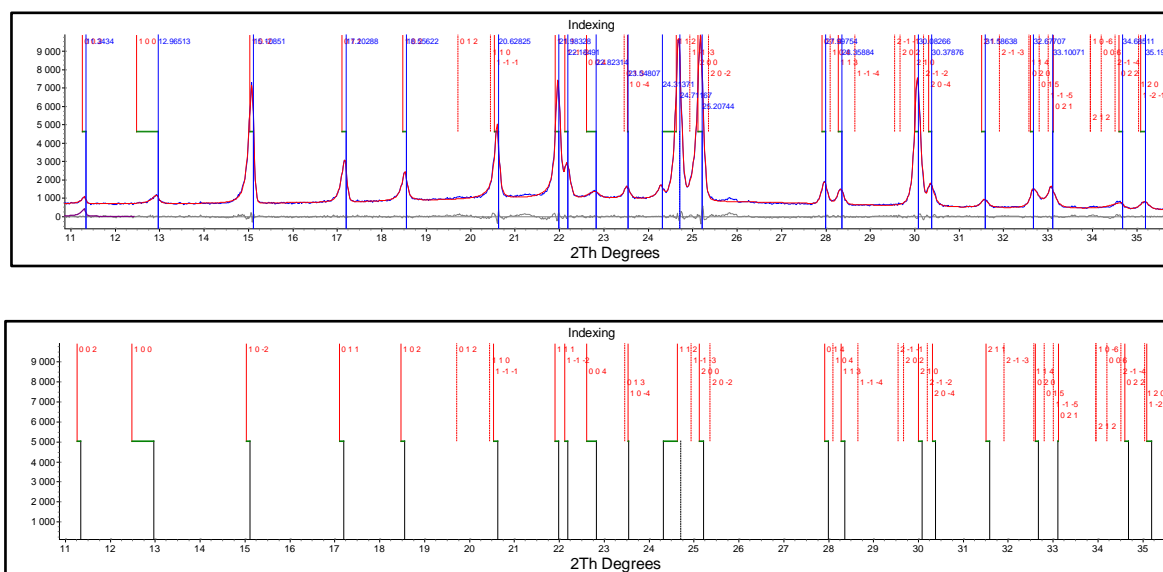


Fig. S5 Variable-temperature PXRD patterns of ABN showing the phase change after 180 K.

(a)



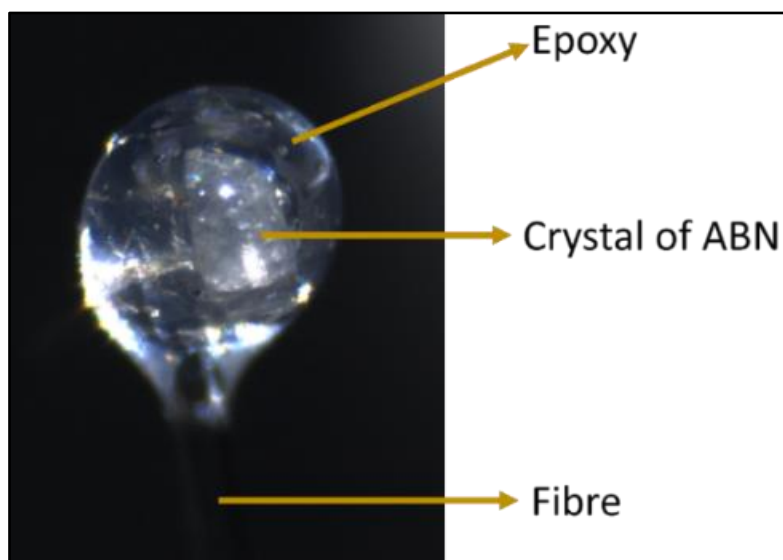


Fig. S7 A single crystal of ABN glued to a glass fibre and covered with epoxy.

Table S1 Crystallographic details for ABN.

Identification code	ABN_300K	ABN_280K	ABN_260K	ABN_240K	ABN_220K	ABN_200K
Empirical formula	C ₇ H ₆ N ₂					
Formula weight/g/mol	118.14	118.14	118.14	118.14	118.14	118.14
Temperature/K	300(2)	280(2)	260(2)	240(2)	220(2)	200(2)
Crystal system	Monoclinic	Monoclinic	Monoclinic	Monoclinic	Monoclinic	Monoclinic
Space group	<i>P</i> 2 ₁ / <i>c</i>					
<i>a</i> /Å	7.3414(5)	7.3198(5)	7.3002(5)	7.2815(6)	7.2662(6)	7.2430(5)
<i>b</i> /Å	5.5181(4)	5.5097(3)	5.5022(3)	5.4951(4)	5.4906(4)	5.4842(4)
<i>c</i> /Å	16.1043(11)	16.0906(11)	16.0771(11)	16.0633(12)	16.0552(13)	16.0426(11)
α /°	90	90.00	90.00	90.00	90.00	90.00
β /°	102.118(2)	102.034(2)	101.968(2)	101.903(2)	101.835(3)	101.8840(10)
γ /°	90	90.00	90.00	90.00	90.00	90.00
Volume/Å ³	637.86(8)	634.67(7)	631.73 (7)	628.91(8)	626.92(8)	623.79(8)
Z	4	4	4	4	4	4
ρ_{calc} /cm ³	1.230	1.236	1.242	1.248	1.252	1.258
μ /mm ⁻¹	0.077	0.078	0.078	0.079	0.079	0.079
F(000)	248	248	248	248	248	248
Crystal size/mm ³	0.63 × 0.44 × 0.16	0.62 × 0.43 × 0.15	0.61 × 0.42 × 0.14	0.60 × 0.41 × 0.13	0.59 × 0.40 × 0.12	0.58 × 0.39 × 0.11
Radiation	MoK α (λ = 0.71073)					
θ range for data collection/°	2.84 to 25.02	2.85 to 25.34	3.92 to 25.35	3.93 to 25.35	3.93 to 25.34	3.94 to 26.02
Index ranges	-8 ≤ <i>h</i> ≤ 8, -6 ≤ <i>k</i> ≤ 6, -19 ≤ <i>l</i> ≤ 19	-8 ≤ <i>h</i> ≤ 8, -6 ≤ <i>k</i> ≤ 6, -19 ≤ <i>l</i> ≤ 19	-8 ≤ <i>h</i> ≤ 8, -6 ≤ <i>k</i> ≤ 6, -19 ≤ <i>l</i> ≤ 19	-8 ≤ <i>h</i> ≤ 8, -6 ≤ <i>k</i> ≤ 6, -19 ≤ <i>l</i> ≤ 19	-8 ≤ <i>h</i> ≤ 8, -6 ≤ <i>k</i> ≤ 6, -19 ≤ <i>l</i> ≤ 19	-8 ≤ <i>h</i> ≤ 8, -6 ≤ <i>k</i> ≤ 6, -19 ≤ <i>l</i> ≤ 19
Reflections collected	9632	9938	9862	9587	9293	9860
Independent reflections	1119 [R _{int} = 0.0344]	1151 [R _{int} = 0.0337]	1146 [R _{int} = 0.0314]	1142 [R _{int} = 0.0279]	1138 [R _{int} = 0.0269]	1206 [R _{int} = 0.0263]
Data/restraints/parameters	1119/0/90	1151 /0/90	1146/0/90	1142/0/90	1138/0/90	1206/0/90
Goodness-of-fit on F ²	1.043	1.078	1.047	1.083	1.065	1.049
Final R indexes [<i>I</i> ≥ 2 σ (<i>I</i>)]	R ₁ = 0.0407, wR ₂ = 0.1013	R ₁ = 0.0403, wR ₂ = 0.1035	R ₁ = 0.0388, wR ₂ = 0.0981	R ₁ = 0.0367, wR ₂ = 0.0942	R ₁ = 0.0350, wR ₂ = 0.087	R ₁ = 0.0357, wR ₂ = 0.0898
Final R indexes [all data]	R ₁ = 0.0522, wR ₂ = 0.1096	R ₁ = 0.0493, wR ₂ = 0.1111	R ₁ = 0.0475, wR ₂ = 0.1053	R ₁ = 0.0436, wR ₂ = 0.1001	R ₁ = 0.0410, wR ₂ = 0.0919	R ₁ = 0.0424, wR ₂ = 0.0946
Largest diff. peak/hole / e Å ⁻³	0.094/-0.12	0.093/-0.118	0.105/-0.119	0.117/-0.122	0.12/-0.098	0.139/-0.137
CCDC Number	1816756	1816754	1816755	1816759	1816758	1816753

Table S1 continued

Identification code	ABN_180K	ABN_160K	ABN_140K	ABN_120K	ABN_100K	ABN_300K_R
Empirical formula	C ₇ H ₆ N ₂					
Formula weight	118.14	118.14	118.14	118.14	118.14	118.14
Temperature/K	180(2)	160(2)	140(2)	120(2)	100(2)	300(2)
Crystal system	Monoclinic	Monoclinic	Monoclinic	Monoclinic	Monoclinic	Monoclinic
Space group	<i>P</i> 2 ₁ / <i>c</i>					
<i>a</i> /Å	7.2228(5)	7.368(2)	7.3455(19)	7.3320(89)	7.3184(18)	7.3645(18)
<i>b</i> /Å	5.4765(4)	5.7105(17)	5.7043(15)	5.7057(14)	5.7059(15)	5.5357(14)
<i>c</i> /Å	16.0273(12)	15.915(5)	15.878(4)	15.859(4)	15.844(4)	16.147(4)
<i>a</i> /°	90.00	90.00	90.00	90.00	90.00	90.00
<i>β</i> /°	101.740(2)	113.088(7)	113.224(6)	113.341(6)	113.439(6)	102.119(6)
<i>γ</i> /°	90.00	90.00	90.00	90.00	90.00	90.00
Volume/Å ³	620.71(8)	616.0(3)	611.4(3)	609.1(3)	607.0(3)	643.60
<i>Z</i>	4	4	4	4	4	4
ρ_{calc} g/cm ³	1.264	1.274	1.283	1.288	1.293	1.219
μ /mm ⁻¹	0.080	0.080	0.081	0.081	0.081	0.077
<i>F</i> (000)	248	248	248	248	248	248
Crystal size/mm ³	0.57 × 0.38 × 0.10	0.56 × 0.37 × 0.09	0.55 × 0.36 × 0.08	0.54 × 0.35 × 0.07	0.53 × 0.34 × 0.06	0.63 × 0.44 × 0.16
Radiation	MoK α (λ = 0.71073)					
θ range for data collection/°	2.88 to 25.34	2.78 to 26.17	3.02 to 26.11	3.03 to 26.11	3.03 to 25.02	2.83 to 26.36
Index ranges	-8 ≤ <i>h</i> ≤ 8, -6 ≤ <i>k</i> ≤ 6, -19 ≤ <i>l</i> ≤ 19	-9 ≤ <i>h</i> ≤ 9, -7 ≤ <i>k</i> ≤ 6, -19 ≤ <i>l</i> ≤ 19	-9 ≤ <i>h</i> ≤ 9, -7 ≤ <i>k</i> ≤ 6, -19 ≤ <i>l</i> ≤ 19	-9 ≤ <i>h</i> ≤ 9, -7 ≤ <i>k</i> ≤ 6, -19 ≤ <i>l</i> ≤ 19	-8 ≤ <i>h</i> ≤ 8, -6 ≤ <i>k</i> ≤ 6, -18 ≤ <i>l</i> ≤ 18	-9 ≤ <i>h</i> ≤ 9, -6 ≤ <i>k</i> ≤ 6, -20 ≤ <i>l</i> ≤ 20
Reflections collected	9721	6188	7099	7218	6483	6483
Independent reflections	1134 [R _{int} = 0.0283]	1208 [R _{int} = 0.1831]	1197 [R _{int} = 0.0420]	1184 [R _{int} = 0.0407]	1056 [R _{int} = 0.0371]	1306 [R _{int} = 0.0420]
Data/restraints/parameters	1134/0/90	1208/0/90	1197/0/90	1184/0/90	1056/0/90	1306/0/90
Goodness-of-fit on F ²	1.067	1.080	1.081	1.102	1.092	1.070
Final R indexes [I ≥ 2 σ (I)]	R ₁ = 0.0344, wR ₂ = 0.0890	R ₁ = 0.0713, wR ₂ = 0.1707	R ₁ = 0.0565, wR ₂ = 0.1270	R ₁ = 0.0560, wR ₂ = 0.1277	R ₁ = 0.0502, wR ₂ = 0.1205	R ₁ = 0.0622, wR ₂ = 0.1360
Final R indexes [all data]	R ₁ = 0.0392, wR ₂ = 0.0929	R ₁ = 0.1001, wR ₂ = 0.1876	R ₁ = 0.0786, wR ₂ = 0.1377	R ₁ = 0.0772, wR ₂ = 0.1383	R ₁ = 0.06769, wR ₂ = 0.1294	R ₁ = 0.1150, wR ₂ = 0.1580
Largest diff. peak/hole / e Å ⁻³	0.131/-0.143	0.315/-0.244	0.201/-0.218	0.219/-0.218	0.200/-0.218	0.119/-0.151
CCDC Number	1816752	1816762	1816750	1816749	1816748	1816757

Table S2 Hydrogen bonding interaction in ABN from 100 K to 300 K

Temperature (K)	100	120	140	160	180	200	220	240	260	280	300	300_R
N1...N2 (Å)	3.1385 (6)	3.1417 (5)	3.1452 (6)	3.1515 (8)	3.2052 (2)	3.2116 (1)	3.2154 (2)	3.2193 (2)	3.2235 (1)	3.2284 (1)	3.2339 (1)	3.2474 (5)
N1-H1B...N2 (°)	159.204 (13)	159.543 (10)	159.471 (11)	161.053 (12)	156.906 (3)	156.929 (3)	156.925 (3)	156.609 (3)	157.406 (2)	157.002 (2)	157.132 (3)	156.718 (9)
C3...N2 (Å)	3.4713 (6)	3.4742 (6)	3.4789 (7)	3.4864 (8)	3.4592 (2)	3.4690 (2)	3.4779 (2)	3.4845 (2)	3.4940 (2)	3.5031 (2)	3.5130 (2)	3.5230 (6)
C3-H3...N2 (°)	144.545 (9)	144.764 (8)	144.906 (9)	145.406 (10)	156.524 (2)	156.643 (2)	156.903 (2)	157.118 (2)	157.395 (2)	157.502 (2)	157.717 (2)	157.992 (8)
C3...i _{C=N} (Å)	3.6209 (7)	3.6249 (6)	3.6300 (7)	3.6431 (8)	3.7806 (2)	3.7886 (2)	3.7968 (2)	3.8022 (2)	3.8098 (2)	3.8185 (2)	3.8276 (2)	3.8399 (6)
N1...i _{Ar} (Å)	3.4049 (7)	3.4113 (7)	3.4213 (7)	3.4318 (8)	3.4383 (2)	3.4486 (2)	3.4615 (2)	3.4703 (2)	3.4810 (2)	3.4935 (2)	3.5044 (2)	3.5158 (7)

Non-standard unit cell setting

In the temperature range 300 to 180 K, the monoclinic space group setting for ABN could be either $P2_1/c$ with a β angle of ca 102° , or $P2_1/n$ with a β angle of ca 104° . The former is the standard setting because its angle is closer to 90° . After the phase transition, the monoclinic crystal system is retained, and the space group settings could be either $P2_1/c$ with a β angle of ca 113° , or $P2_1/n$ with a β angle of ca 94° . In this case, the latter is the standard setting. However, accepting the standard setting for the low temperature phase does not facilitate direct comparison of the structures before and after the transition. We therefore enforced the $P2_1/c$ setting for the low temperature phase because this choice facilitates our understanding of the transition that accompanies the thermosalient event.

Thermal expansion

This study investigates two enantiotropic polymorphs of ABN in the monoclinic crystal system. Since the three crystallographic axes are not orthogonal to one another the principal axis strain calculator (PASCAL program)⁷ was used to determine the linear thermal expansion coefficients along all the three principal axes, as well as the volumetric thermal expansion coefficient.

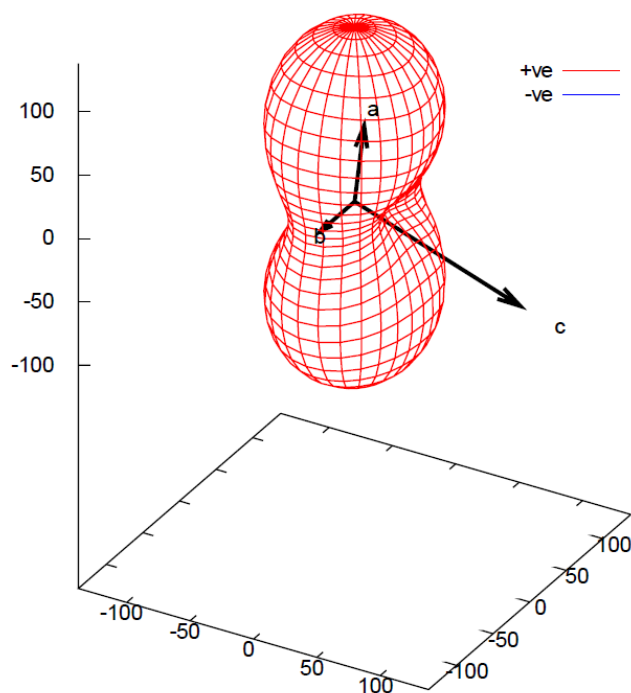


Fig. S8 Expansivity indicatrix (300 to 180 K).

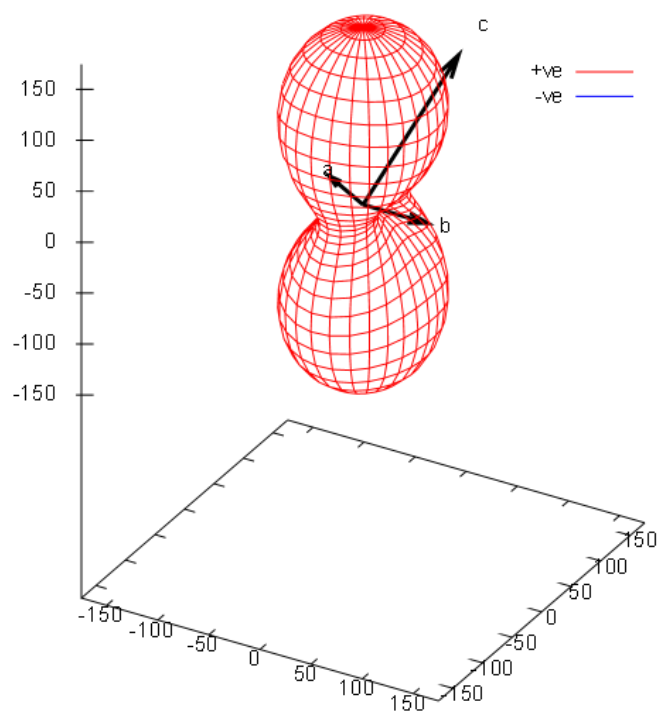


Fig. S9 Expansivity indicatrix (160 to 100 K).

Table S3 Thermal expansion coefficients α_{X1} , α_{X2} , and α_{X3} and volumetric thermal expansion coefficients (α_V), with the percentage changes in length and volume.

Purely organic crystal	Temp(K)	$\alpha_{X1}(\text{MK}^{-1})$	$\alpha_{X2}(\text{MK}^{-1})$	$\alpha_{X3}(\text{MK}^{-1})$	$\alpha_V(\text{MK}^{-1})$	% change in length along X1	% change in length along X2	% change in length along X3	% change in volume
ABN	100 – 160	10.87	54.76	174.69	250.04	0.08	0.34	1.06	1.5
	180 – 300	24.76	61.34	138.19	225.07	0.31	0.76	1.69	3.0

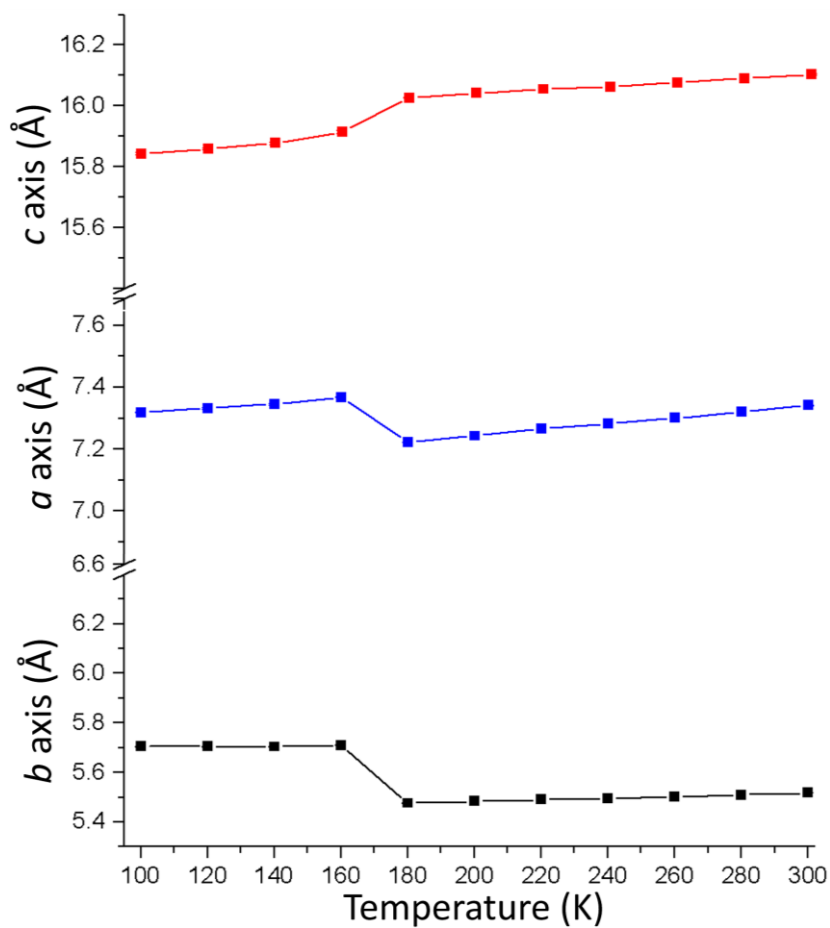


Fig. S10 Variation in the unit cell dimension showing the phase transition between 160 and 180 K.

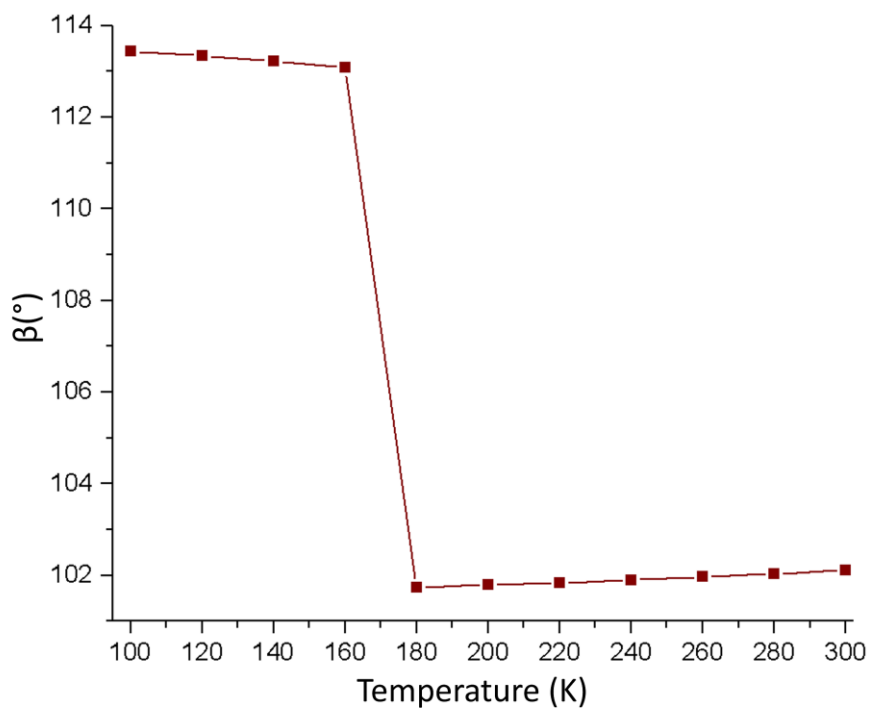


Fig. S11 Variation in the β angle showing the phase transition between 160 and 180 K

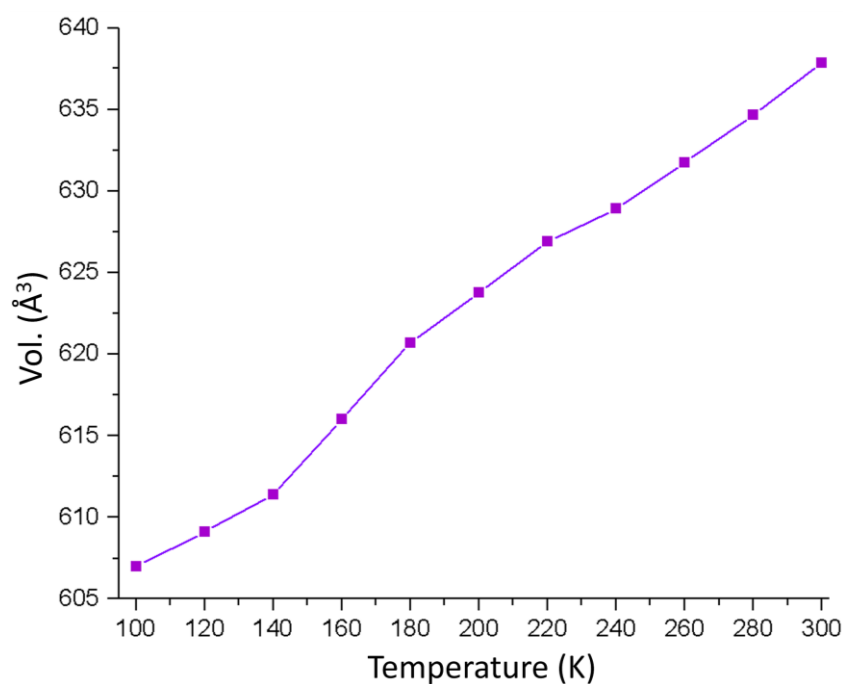


Fig. S12 Variation in unit cell volume of ABN with temperature.

Hirshfeld surface analysis

The program CrystalExplorer⁸ (Version 3.1) was used to generate Hirshfeld surfaces (d_{norm}) to indicate the intermolecular interactions for a molecule of ABN in the structures determined at 180 and 160 K. Animations of the surfaces and the corresponding interacting molecules are shown in Videos S3 and S4, respectively.

Overlay of bilayers

In order to assess the similarity of the bilayers in the structures at 180 and 160 K, subsets of the two structures were overlaid using Materials Studio.⁹ The RMS difference for a 4×2 subset of molecules within the bilayers (represented with thicker bonds in Fig. S12) is 0.176 Å.

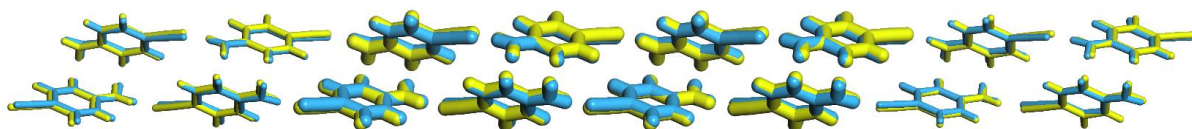


Fig. S13 Overlay of the bilayers showing negligible change in the internal arrangement before and after phase change (Yellow, 180 K; Blue, 160 K).

Theoretical investigation

Hydrogen-atom positions were optimised in *P1* using the DMol³ code as implemented in Materials Studio with non-hydrogen atoms constrained to their crystallographic positions.¹⁰ The density functional theory (DFT) generalised gradient approximation of Perdew-Burke-Ernzerhof (PBE)¹¹ in combination with Grimme's DFT-D dispersion correction¹² was employed. The double numeric plus polarization basis set (DNP, version 4.4) was employed with an orbital cut-off of 3.7 Å. Integration in the reciprocal lattice was performed using a Monkhorst-Pack grid¹³ with a k-point separation of 0.07 Å⁻¹ and self-consistent field convergence was set to 1.0×10^{-6} au. A hexadecapole multipolar expansion¹⁴ and 20% admixture of the charge density was applied in conjunction with a DIIS (direct inversion in an iterative subspace) size of 6 to speed up convergence.¹⁵ Geometry optimization convergence tolerances on energy, maximum force and maximum displacement were set to 1.0×10^{-5} au, 0.002 Ha Å⁻¹ and 0.005 Å, respectively.

Lattice energies were calculated according to the following formula:

$$E_{\text{lattice}} = E_{\text{crystal}} - Z \times E_{\text{reference}}$$

where *Z* represents the number of symmetry operators present in the space group – four for *P2₁/c*. Although trends should be maintained, the choice of reference system affects the absolute values of lattice energies. Removing three ABN molecules from the *P1* geometry-optimised unit cell yielded periodic reference {**ABN**} while subsequent deletion of the unit cell yielded molecular reference (**ABN**). Single point energy evaluations were carried out at the same level of theory as hydrogen-atom geometry optimisations to afford the results given in Figure S14.

A comparison of $E_{\text{lattice}}^{(\bullet)}$ (●) and $E_{\text{lattice}}^{\{\text{ABN}\}}$ (○) shows a similar downward trend upon cooling ABN before and after the phase change; however, an opposite change is observed during the phase change between the 180 and 160 K structures. The periodic aromatic- π interaction along the *b* axis, denoted as $\{\pi_{\text{Ar}} \cdots \pi_{\text{Ar}}\}_{\text{b}}$, is calculated as the difference between the single point energy of {**ABN**} and the single point energy of the system comprising one ABN molecule within a unit cell of which the *b*-axis length is doubled, designated {**ABN *b* × 2**}:

$$E_{\text{int}}^{\{\pi_{\text{Ar}} \cdots \pi_{\text{Ar}}\}} = E_{\{\text{ABN}\}} - E_{\{\text{ABN } b \times 2\}}$$

It is interesting to note that the $\{i_{\text{Ar}} \cdots i_{\text{Ar}}\}_{\text{b}}$ interaction (○) becomes more favourable notwithstanding a lengthening of the *b* axis upon cooling. Taking this principal intermolecular interaction into account, $E_{\text{lattice}}^{\{\text{ABN } b \times 2\}}$ (Δ) is found to closely trace $E_{\text{lattice}}^{(\bullet)}$ (●).

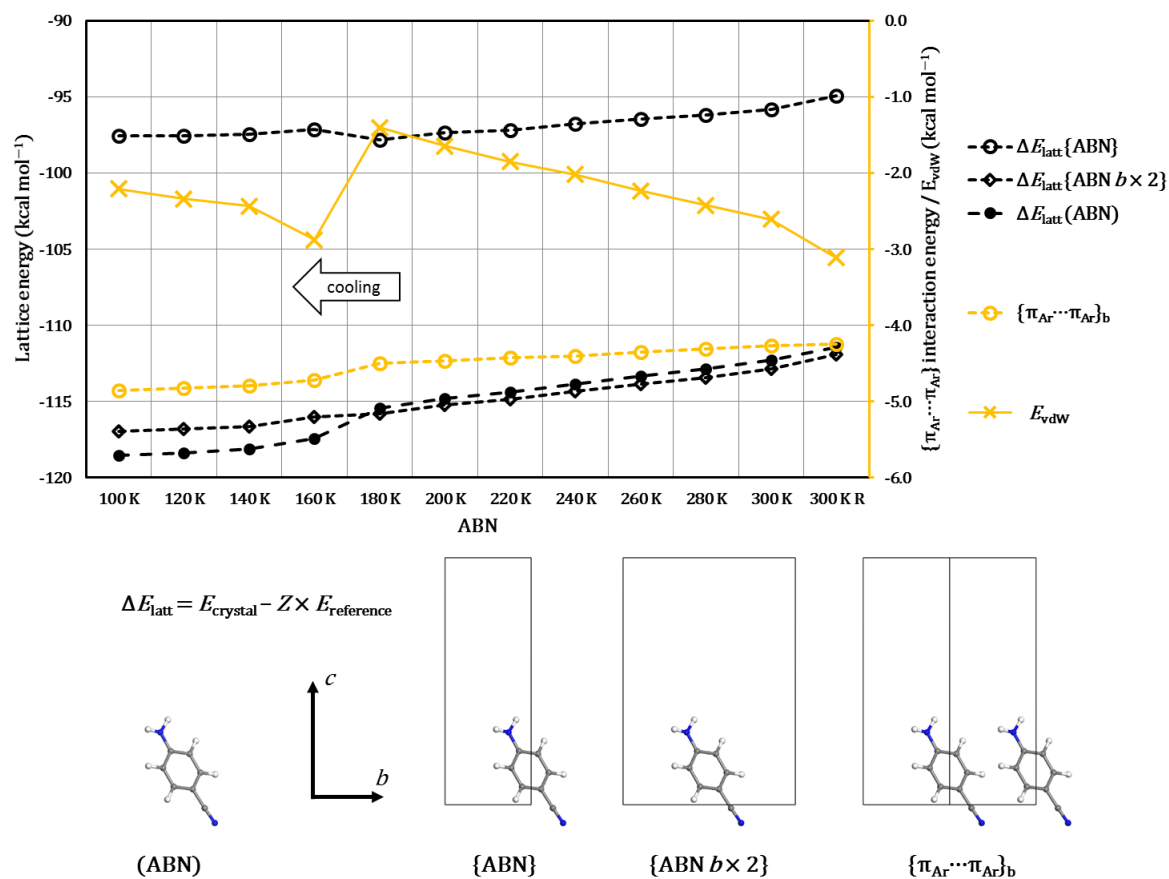


Fig. S14 Comparison of lattice energies calculated using different reference systems. A single ABN in a unit cell with the *b*-axis length doubled, $\{\text{ABN } b \times 2\}$, yields the same lattice energy as that calculated using an isolated ABN molecule, (ABN). Also shown is the change in the strength of the $\{\pi_{\text{Ar}}\cdots\pi_{\text{Ar}}\}_b$ intermolecular (○) and the non-bond van der Waals (×) interactions is.

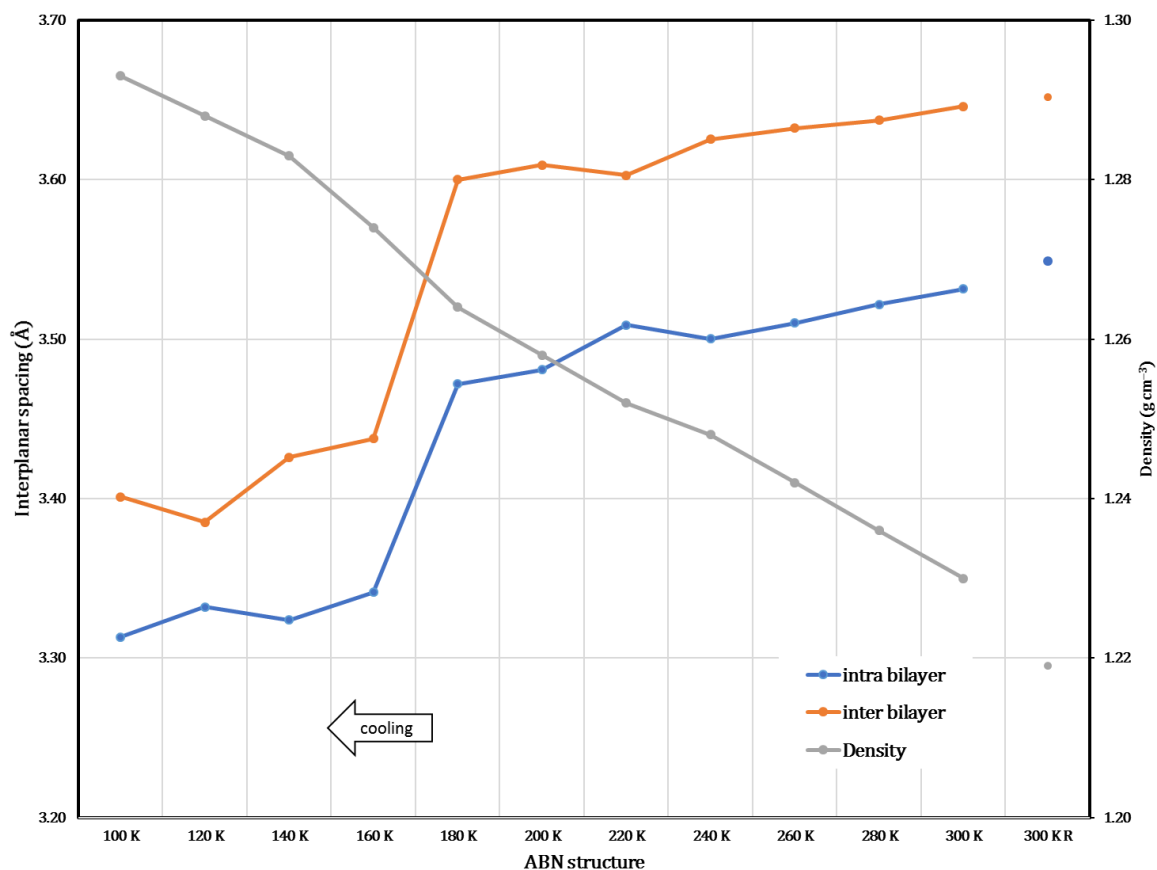


Fig. S15 Comparison of inter- and intra-bilayer spacing (calculated as planes through the aromatic ring centroids) as a function of temperature. Also shown is the trend in calculated density.

The $\{\pi_{Ar} \cdots \pi_{Ar}\}_b$ intermolecular interaction becomes more favourable after the phase due to a reduction of the spacing between mean planes through the ABN molecules, $P_{x,y,z} \cdots P_{x,y+1,z}$ (Table S4).

Table S4 Interplanar and centroid_{Ar}⋯centroid_{Ar} distances involved in principal $\pi \cdots \pi$ intermolecular interactions (P = aromatic mean plane, i_{Ar} = ring centroid, distances in Å).

Temp/K	100	120	140	160	180	200	220	240	260	280	300	300_R
$P_{x,y,z} \cdots P_{x,y+1,z}$	2.49	2.50	2.52	2.53	2.78	2.79	2.80	2.80	2.81	2.82	2.83	2.84
$i_{Ar} \cdots i_{Ar}$	5.71	5.71	5.70	5.71	5.48	5.48	5.49	5.50	5.50	5.51	5.52	5.54
$P_{x,y,z} \cdots P_{1-x,1-y,1-z}$	3.47	3.48	3.49	3.50	3.60	3.61	3.62	3.62	3.63	3.63	3.64	3.65
$i_{Ar} \cdots i_{Ar}$	4.12	4.13	4.15	4.17	5.18	5.19	5.19	5.19	5.19	5.19	5.19	5.20

Molecular Mechanics single point energy evaluations of the hydrogen-atom optimised structures were carried out using the Forcite code of Materials Studio employing the COMPASS force field¹⁶ with force-field assigned charges and Ewald summation.¹⁷

Table S5 Summary of contributions to the Molecular Mechanics total energy.

Temp (K)	100K	120K	140K	160K	180K	200K	220K	240K	260K	280K	300K	300K_R
Energy (kcal mol ⁻¹)												
Total	231.0024	230.4255	229.8857	228.075	222.6462	222.7126	222.3242	222.6924	222.4117	222.1977	222.2181	220.8533
Valence	21.827	21.685	21.648	20.907	22.782	23.217	23.254	23.703	23.739	23.833	24.043	23.448
Valence (diagonal terms)	15.399	15.32	15.316	15.254	15.853	15.816	15.825	15.732	15.648	15.618	15.564	15.481
Bond	1.617	1.614	1.608	1.598	1.333	1.324	1.321	1.307	1.298	1.293	1.289	1.304
Angle	9.33	9.31	9.399	9.301	12.421	12.332	12.48	12.215	12.142	12.108	12.057	11.579
Torsion	3.133	3.085	3.027	3.056	1.519	1.559	1.466	1.59	1.578	1.588	1.584	1.844
Inversion	1.319	1.311	1.282	1.299	0.581	0.601	0.559	0.62	0.629	0.629	0.634	0.754
Valence (cross terms)	6.428	6.365	6.332	5.653	6.929	7.401	7.429	7.971	8.091	8.215	8.479	7.967
Stretch-Stretch	-0.011	-0.013	-0.014	-0.01	-0.01	-0.009	-0.01	-0.009	-0.009	-0.01	-0.009	-0.006
Stretch-Bend-Stretch	-0.678	-0.741	-0.856	-0.656	-0.957	-0.891	-1.02	-0.955	-0.97	-1.012	-1.005	-0.658
Stretch-Torsion-Stretch	4.14	4.357	4.606	3.745	5.257	5.549	5.915	6.301	6.572	6.851	7.191	5.823
Separated-Stretch-Stretch	-0.034	-0.036	-0.038	-0.03	-0.042	-0.045	-0.048	-0.051	-0.053	-0.055	-0.057	-0.047
Torsion-Stretch	-1.853	-1.955	-2.094	-1.952	-2.082	-1.993	-2.134	-2.058	-2.104	-2.156	-2.163	-1.787
Bend-Bend	-1.594	-1.604	-1.632	-1.612	-2.28	-2.26	-2.308	-2.243	-2.235	-2.237	-2.233	-2.109
Torsion-Bend-Bend	0.042	0.036	0.036	0.032	0.052	0.05	0.051	0.052	0.051	0.05	0.048	0.052
Bend-Torsion-Bend	6.416	6.321	6.324	6.137	6.992	7	6.984	6.933	6.839	6.782	6.707	6.699
Non-bond	209.176	208.74	208.238	207.168	199.864	199.496	199.07	198.99	198.673	198.365	198.176	197.406
Van der Waals	-2.209	-2.338	-2.436	-2.875	-1.403	-1.646	-1.853	-2.02	-2.235	-2.422	-2.607	-3.11
Electrostatic	211.385	211.078	210.673	210.043	201.268	201.141	200.923	201.01	200.908	200.787	200.782	200.516

Trends in the strengths of principal directional intermolecular interaction energies were subsequently investigated at the DFT level of theory. Each ABN molecule acts as a donor and acceptor for three principal intermolecular interactions of type $\text{N-H}\cdots\text{N}\equiv\text{C}$, $\text{N-H}\cdots\pi_{\text{Ar}}$ and $\text{C-H}\cdots\pi_{\text{C}\equiv\text{N}}$ as shown in Figure S16. Two offset aromatic- π interactions are present: $\{\pi_{\text{Ar}}\cdots\pi_{\text{Ar}}\}_b$ along the b axis and $\{\pi_{\text{Ar}}\cdots\pi_{\text{Ar}}\}$ between bilayers. Table S4 shows the reduction in the $\text{P}_{x,y,z}\cdots\text{P}_{x,y+1,z}$ and $\text{P}_{x,y,z}\cdots\text{P}_{1-x,1-y,1-z}$ mean plane separation.

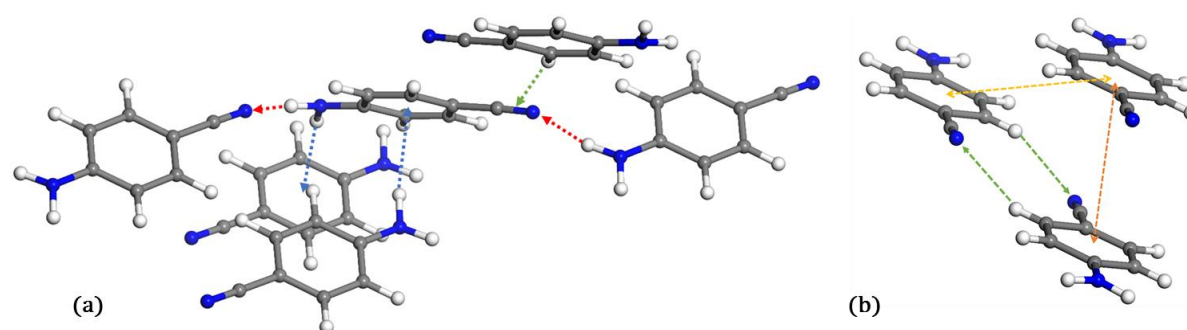


Fig. S16 (a) The six principal directional intermolecular interactions each ABN molecule is involved in: $\text{N-H}\cdots\text{N}\equiv\text{C}$ (red, along [001]), $\text{N-H}\cdots\pi_{\text{Ar}}$ (blue) and $\text{C-H}\cdots\pi_{\text{C}\equiv\text{N}}$ (green, to the same molecule). (b) Two offset $\{\pi_{\text{Ar}}\cdots\pi_{\text{Ar}}\}_b$ (yellow, along [010]) and $\{\pi_{\text{Ar}}\cdots\pi_{\text{Ar}}\}$ (orange) interactions.

Molecular and periodic interaction energies used (**ABN**) and **{ABN}** as reference system, respectively. Figure S17 depicts the model structures used in the calculation of periodic E_{int} values, while *bimolecular* models were employed in determining molecular E_{int} values. Note that **{ABN}** already encompasses the $\{\pi_{\text{Ar}} \cdots \pi_{\text{Ar}}\}_{\text{b}}$ interaction present in the periodic model structures. Figures S18 and S19 summarise all E_{int} values.

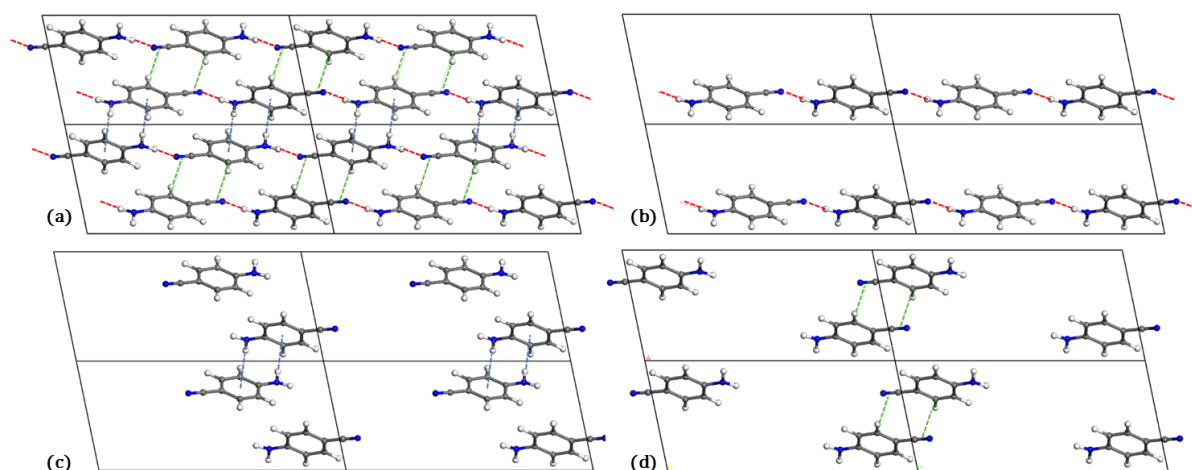


Fig. S17 (a) Packing diagram of the ABN collected at 180 K and model structures used for the calculation of the strength of the (b) intralayer $\text{N-H} \cdots \text{N}\equiv\text{C}$ (red), (c) intrabilayer $\text{N-H} \cdots \pi_{\text{Ar}}$ (blue) and (d) interbilayer $\text{C-H} \cdots \pi_{\text{C}\equiv\text{N}}$ (green) periodic intermolecular interactions. View: [010]

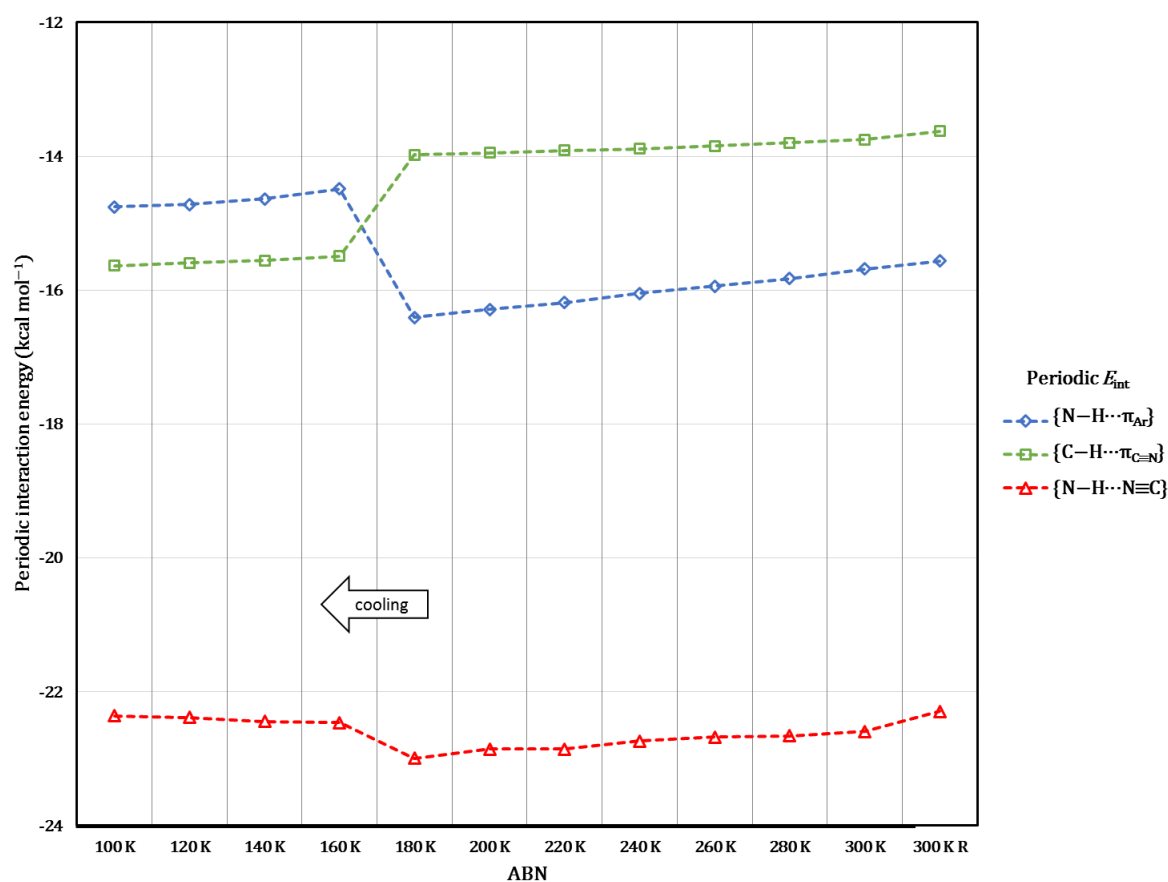


Fig. S18 Plot of periodic interaction energies of principal intermolecular interactions.

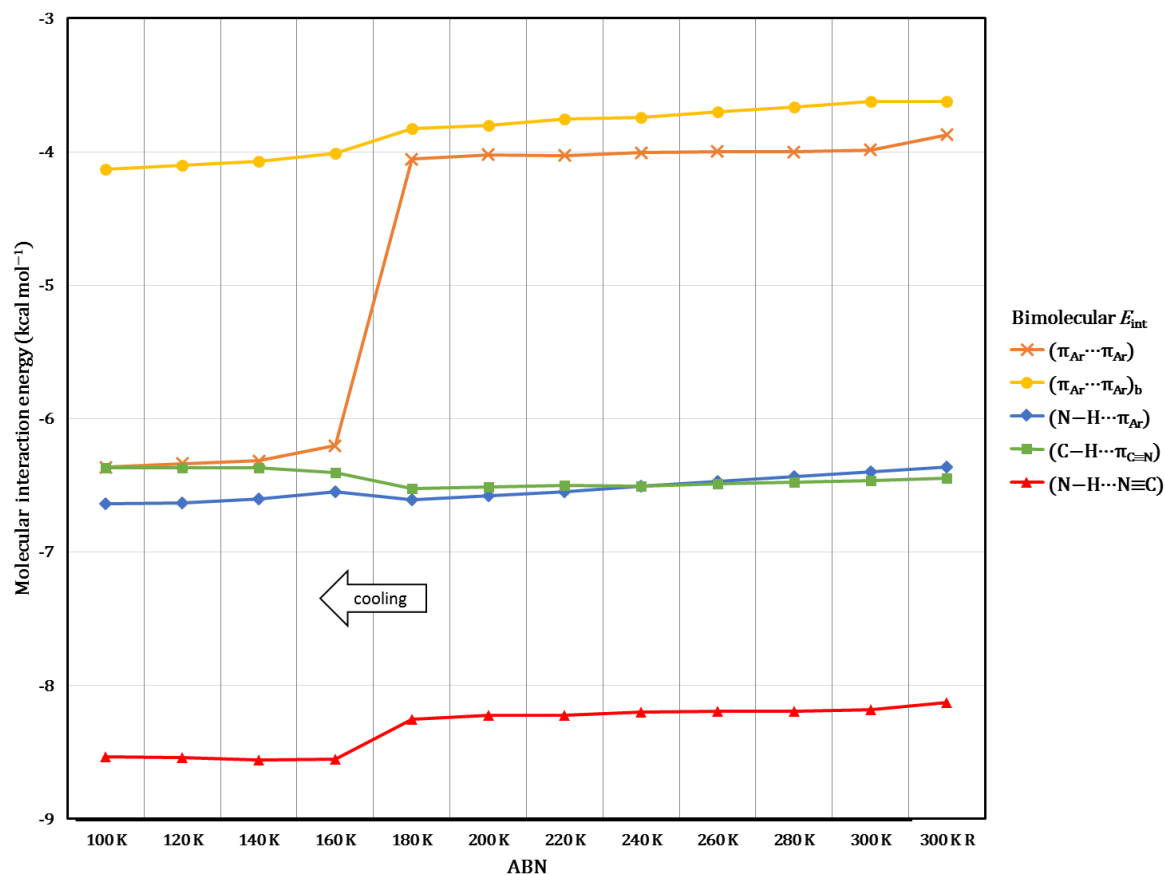


Fig. S19 Plot of molecular interaction energies of principal intermolecular interactions.

The molecular ($\pi_{Ar}\cdots\pi_{Ar}$)_b interaction (●) follows a similar trend as the periodic $\{\pi_{Ar}\cdots\pi_{Ar}\}$ _b (○, cf. Fig. S14). The strengthening of the periodic C-H $\cdots\pi_{C\equiv N}$ interaction is not mirrored in the molecular case due to the admixture of the $\{\pi_{Ar}\cdots\pi_{Ar}\}$ interaction. Thus, $E_{int}^{\{C-H\cdots\pi_{C\equiv N}\}}|_{\square} \approx E_{int}^{(C-H\cdots\pi_{C\equiv N})}|_{\square} + E_{int}^{(\pi_{Ar}\cdots\pi_{Ar})}|_{\times}$. Whereas the molecular $E_{int}^{(N-H\cdots N\equiv C)}|_{\blacktriangle}$ becomes more favourable during the 180 to 160 K thermosalient phase change, the periodic $E_{int}^{\{N-H\cdots N\equiv C\}}|_{\blacktriangle}$ shows a destabilisation. *Trimolecular* models were used to approximate crystal field polarization effects to yield the molecular interaction energies shown in Figure S20. The deconvoluted E_{int} are all more favourable than their bimolecular counterpart and show a more pronounced change over the phase change. The deconvoluted $E_{int}^{(N-H\cdots N\equiv C)}|_{\blacktriangle}$ (Fig. S20(b)) now follows the same trend as $E_{int}^{\{N-H\cdots N\equiv C\}}|_{\blacktriangle}$ (cf. Fig. S18), highlighting the cooperative effect of intermolecular interactions in crystal structures.

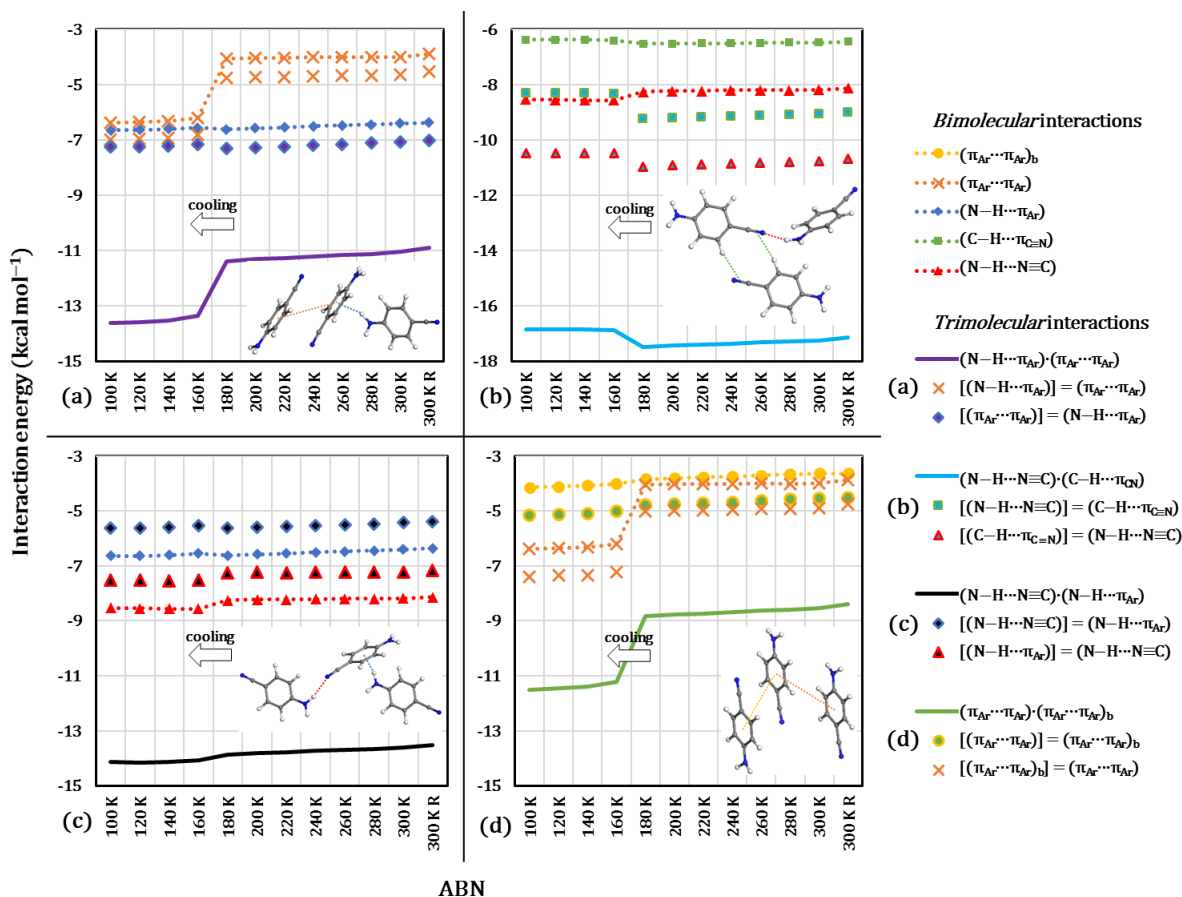


Fig. S20 Deconvoluted interaction energies calculated from *trimolecular* representations. The corresponding bimolecular interaction energies are plotted for each combination.

The 2.2 kcal mol⁻¹ strengthening of the interbilayer ($\pi_{Ar} \cdots \pi_{Ar}$) interaction (✕, Fig. S19) can be considered a major driving force for the 180 to 160 K phase change. A similar strengthening of the intrabilayer N-H \cdots π_{Ar} interaction (◇, Fig. S18) might account for the reversal of the phase change. However, a balance between directional intermolecular interactions and profuse non-directional van der Waals forces determines the physical conditions that bring about the thermosalient phase change.

References

1. TOPAS, V4.2, *General Profile and Structure Analysis Software for Powder Diffraction Data Users' Manual*; Bruker, AXS: Karlsruhe, 2009.
2. SAINT Data Reduction Software, Version 2017.3-RC2; Bruker AXS 2005-2017.
3. SADABS, Version 2.05; Bruker AXS Inc.: Madison, WI, 2002.
4. R. H. Blessing, *An Empirical Correction for Absorption Anisotropy*, *Acta Crystallogr., Sect. A: Found. Crystallogr.*, 1995, **51**, 33.
5. G. M. Sheldrick, *A Short History of SHELX*. *Acta Crystallogr., Sect. A: Found. Crystallogr.*, 2008, **64**, 112.

6. L. Barbour, X-Seed – A Software Tool for Supramolecular Crystallography. *J. Supramol. Chem.*, 2001, **1**, 189.
7. J. Cliffe and A. L. Goodwin, *J. Appl. Crystallogr.*, 2012, **45**, 1321.
8. M.A. Spackman, D. Jayatilaka, *CrystEngComm*, 2009, **11**, 19.
9. Dassault Systèmes BIOVIA Materials Studio, Release 18, San Diego: Dassault Systèmes, 2017.
10. B. Delley, *J. Chem. Phys.*, 2000, **113**, 7756.
11. J. P. Perdew, K. Burke and M. Ernzerhof, *Phys. Rev. Lett.*, 1996, **77**, 3865.
12. S. Grimme, *J. Comput. Chem.*, 2006, **27**, 1787.
13. H. J. Monkhorst and J. D. Pack, *Phys. Rev. B*, 1976, **13**, 5188.
14. B. Delley, *J. Chem. Phys.*, 1990, **92**, 508
15. P. Pulay, *Chem. Phys. Lett.*, 1980, **73**, 393
16. H. Sun, Z. Jin, C. Yang, R. L. C. Akkermans, S. H. Robertson, N. A. Spenley, S. Miller, S. M. Todd, *J. Mol. Model.*, 2016, **22**, 47.
17. M. P. Tosi, *Solid State Physics*, 1964, **16**, 107.